Laminar flow field in a viscous liquid impinging jet confined by inclined plane walls

A.S. Cavadas*, F.T. Pinho, J.B.L.M. Campos

Centro de Estudos de Fenómenos de Transporte, Faculdade de Engenharia da Universidade do Porto, Rua Dr. Roberto Frias s/n, 4200-465 Porto, Portugal

ARTICLE INFO

ABSTRACT

An experimental and numerical investigation was carried out to characterize the isothermal laminar flow of a liquid impinging jet confined by inclined plane walls and emanating from a rectangular duct, where the flow was allowed to become fully-developed. The rectangular duct has an aspect ratio of 13, the plane walls opposite to the impinging jet have an inclination of $12°$ and the nozzle-to-plate distance (D) is very short, $D/H = 0.8$. The presence of the impact plate is felt upstream the nozzle, inside the rectangular duct, up to $x/H = -0.4$. The flow in the cell is symmetric relative to the *x-y* and *x-z* center planes and near the inclined walls the flow separates for Reynolds numbers higher than 208, except close to the side walls where the flow remains attached. The length of the separated flow region, L_R, measured along the inclined wall, is constant in the central portion of the channel with $L_R/H = 0.35$ for $Re = 275$ and dropping to zero before reaching the side walls. The recirculation length increases with the Reynolds number and with the thickness of the outlet channel. There is a three-dimensional effect associated with the finite slenderness of the geometry. It consists of spiraling secondary motions away from the central symmetry plane and toward the side walls, where the fluid merges with the main flow creating a local wall jet, as is discussed in detail.

© 2012 Elsevier Masson SAS. All rights reserved.

1. Introduction

Confined impinging jets are frequently used to enhance heat and mass transfer since the high velocity fluid impinging the solid surface creates a very thin boundary layer in addition to the beneficial effect of convective transport. Impinging jets are found in various industrial processes and systems such as in paper and textile drying, steel mills, cooling of turbine blades, tempering of glass and cooling of electronic components. Hence, they have been the subject of many investigations to characterize the flow, as well as the corresponding heat and mass transfer fluxes, and the relation between these fluxes, geometric parameters and inlet flow conditions in particular for the turbulent regime. Early experimental contributions were those of Gardon and Akfirat [10,11] and Korger and Krizek [15], amongst others. With the advent of accurate optical diagnostics in fluid mechanics such as laser-Doppler anemometry (LDA), and more recently particle image velocimetry (PIV), detailed experimental programs have extensively documented some basic flows.

The most obvious way of increasing heat and mass transfer is the promotion of turbulence. Recent investigations on turbulent impinging jets are the extensive turbulence statistics characterization of a circular jet flow impinging on a standing plate by Nishino et al. [23], of Sakakibara et al. [30], for a plane jet and of Senter and Solliec [31] for a slot jet impinging on a moving surface. These flows are also extensively used in the context of two-phase fluids as in spray cooling or in liquid fuel delivery in internal combustion engines, which has fostered a large body of research on dilute and dense spray atomization. A state of the art review in spray cooling is found in Kim [14], whereas Panão [26] reviews spray atomization. Cotler at al. [8] provided a study on the modern application of two-phase impinging jets to electronic cooling systems.

Liquid single-phase impinging jets are usually either submerged or free-surface jets. In submerged jets, very common with air, the liquid fluid issues into a region containing the same fluid at rest, whereas in free-surface jets the liquid jet is surrounded by ambient air or gas. Submerged jets can be unconfined or confined by a surface; in the latter case, there is usually a plate attached to the

---

* Corresponding author.
  E-mail addresses: adelioc@fe.up.pt (A.S. Cavadas), fpinho@fe.up.pt (F.T. Pinho), jmc@fe.up.pt (J.B.L.M. Campos).

Nomenclature

AR	aspect ratio
D	nozzle-to-plate distance
D_H	hydraulic diameter
g	standard earth gravity
h	height of the channel exit
H	height of rectangular duct
LDA	Laser Doppler Anemometer
Re	Reynolds Number based on the hydraulic diameter of the rectangular duct and on the bulk velocity
U	area-averaged bulk velocity in the rectangular duct
u	fluid velocity along the x direction
v	fluid velocity along the y direction
W	width of the rectangular duct

Greek symbols

α	angle of the sloping wall
μ	fluid viscosity
ρ	fluid density
σ	area ratio between the entrance and the exit channels $\sigma = A_1/A_2$

Superscripts, subscripts and special symbols

a^*	nondimensional streamwise advective acceleration
α_1	profile shape factor for energy at plane 1(cf. Fig. 2(b))
α_2	profile shape factor for energy at plane 2 (cf. Fig. 2(b))
f_1	friction factor at inlet channel (cf. Fig. 2(b))
f_2	friction factor at outlet channel (cf. Fig. 2(b))
fx	expansion (or contraction) factors for mesh spacing in the x direction

fy	expansion (or contraction) factors for mesh spacing in the y direction
fz	expansion (or contraction) factors for mesh spacing in the z direction
L_1	length of the computational inlet channel (cf. Fig. 2(b))
L_2	length of the computational outlet channel (cf. Fig. 2(b))
L_R	recirculation length measured in the inclined plane wall
Nx	number of internal cells in the x direction
Ny	number of internal cells in the y direction
Nz	number of internal cells in the z direction
P_0	stagnation pressure
$\dot{Q}_{in}$	volumetric flow rate
ΔP	dimensionless excess pressure loss
Δp_{F1}	wall friction pressure loss at the entrance channel
Δp_{F2}	wall friction pressure loss at the exit channel
P_{01}	pressure upstream of the cell at plane 01(cf. Fig. 2(b))
P_{02}	pressure downstream of the cell at plane 02(cf. Fig. 2(b))
P_1	pressure at plane 1(cf. Fig. 2(b))
P_2	pressure at plane 2(cf. Fig. 2(b))
$\dot{\varepsilon}^*$	nondimensional variation of the streamwise velocity also denote normalized strain rate
U_0	fully-developed velocity value
U_1	bulk velocity in the rectangular channel, also plane 1 (cf. Fig. 2(b))
V_2	bulk velocity in plane 2 (cf. Fig. 2(b))
u_c	velocity along the cell axis
τ_{xy}	shear stress

nozzle and in the most frequent configuration the plate is parallel to the impinging surface.

Regarding free jets Quinn [29] studied the influence of aspect ratio (AR) for turbulent rectangular free jets with AR = 2, 5 and 10. His results show that as the aspect ratio increases, the mixture velocity (liquid and ambient air) increases, while the length of the jet core decreases. Recently, Zhou and Lee [42] measured the flow field and the heat transfer coefficient in a jet with an aspect ratio of 4, at Reynolds numbers between 2715 and 25,000 and for ejector clearances between 1 and 30 heights of the rectangular duct. They quantified the variation of the average and local Nusselt numbers with the Reynolds number, the clearance and the turbulence intensity. In particular, they observed dramatic changes in the stagnation zone. Yang et al. [41] studied experimentally the effect of the shape of the impinging surface; they found higher heat transfer rates for impingement on semi-cylindrical concave surfaces than on planar surfaces on account of the different flow patterns especially away from the stagnation region.

Wolf et al. [40] studied free impinging water jets with a uniform velocity distribution exiting the ejector. This inlet velocity distribution was found to enhance significantly the heat transfer, but this increase was also attributed to increasing turbulence levels. Narayanan et al. [21] also investigated the flow pattern and heat transfer of plane impinging jets addressing specifically the effect of ejector clearance, which was varied between 3.5 and 5 hydraulic diameters. They measured the mean and turbulent velocity fields, the pressure fluctuations and the heat transfer on the impinging plate to show a high heat transfer rate in the impinging zone, followed by a local minimum and then a second maximum at the wall region, at 1.5 and 3.2 hydraulic diameters downstream of the jet center, respectively. The position of the second heat transfer rate

peak coincided with a local maximum of velocity fluctuations. Chen and Modi [7] investigated also rectangular impinging turbulent jets aimed to quantify the mass transfer rate.

However, in many cases the fluids are very viscous, or the geometries are small, so the flow cannot sustain turbulence and the flow regime is inevitably laminar. Our ultimate aim is the investigation of the flow characteristics of impinging rectangular jets for non-Newtonian fluids and a comparison with the corresponding Newtonian flow cases. The jet confinement is by inclined plane walls, which extend from the exit of a rectangular duct to a short distance above the impinging plate. In the present paper, we focus exclusively on Newtonian fluids in the laminar regime and we compare the results with turbulent data for Newtonian fluids. Since the viscous fluids are usually solutions of viscous additives or suspensions of particles, their viscosities can be significantly higher than those of the pure solvent, unless the solvent is already a viscous fluid (such as Boger fluids). However, if the flow geometries are of small size, the fluids do not need to be very viscous. With the advent of cheap micro-manufacturing and the consequent widespread use of microfluidics interest on laminar flows is growing again. Here, even flows of water take place at low Reynolds numbers, well inside the laminar flow regime [22]. For instance, advanced computing systems dissipate so much energy that classical gas cooling is insufficient to remove the dissipated energy and liquid flows in microchannels are used for new compact heat exchangers.

An early study on confined impinging jets with inclined walls is by Garimella and Rice [12], who investigated circular jets confined by a conical wall. They divided the impinging jet flow field into three regions: the free-jet region, the impingement region and the wall region. The flow in the free-jet region is axial and it is not

affected by the presence of the impinging plate. The axial velocity starts to decay at the nozzle exit, provided the nozzle-to-plate distance is not too small, and the jet spreads to the surroundings before the impingement. In this respect Gardon and Akfirat [10], and Martin [17] had shown earlier that the flow of turbulent jets starts to be affected by the impinging plate at approximately 1.2 nozzle diameters from this surface. In the present study, the clearance between the duct and the plate is very short, about 20% of the duct height, and consequently the presence of the plate is felt well inside the duct, as will be shown later. At the impingement region, the fluid strongly decelerates and is forced to change its direction, flowing to the cell exit after passing through the wall region where a boundary layer develops.

More recently, Miranda and Campos [19,20] performed various studies in an impinging jet confined by a conical wall, in the laminar and transitional regimes, and the present contribution is a follow-up to these works related to a rectangular jet under laminar flow conditions. Miranda and Campos [19] showed that the flow field and mass transfer in the conical cell was similar to that in a cylindrical cell (parallel confinement with the flow spreading in the radial direction from the center) and that the flow and mass transfer characteristics could be divided into two zones: impact zone and wall zone. They showed the existence of a recirculation zone attached to the inclined wall (principal recirculation) and a second small recirculation zone at the impinging plate affecting considerably the flow in the exit when the flow was laminar. They complemented their measurements with an extensive numerical study for laminar flow and observed from these numerical investigations that when the imposed velocity profile at the entrance of the cell was not developed, the second recirculation zone would cease to exist. They also concluded that the size of the main recirculation zone varied in the inverse proportion to the slope of the confinement wall. An important phenomenon in membrane separation cells is the reduction of the concentration polarization by impinging jets confined by the conical wall, which was also investigated in [20]. While the high velocity wall jet attached to the impinging plate reduced this phenomenon, the conical wall was found to induce a small contact area for separation processes by permeation. They suggested that an improvement in the operation of the cell would result from the use of a rectangular geometry with confinement by inclined plane walls. The use of rectangular jets results in a higher area of impact and permeation, thus increasing the permeate flux and the productivity of the separation and these conclusions were an additional motivation for the present investigation.

It is clear from this review that in spite of the large body of literature on confined impinging jets, there is a lack of information regarding laminar planar impinging jet flows confined by inclined walls for Newtonian fluids and even more so when fluids have a non-Newtonian rheological behavior. Consequently, the objective of this work is the investigation of the laminar flow hydrodynamics for Newtonian fluids as a preliminary step toward the future investigation of the corresponding non-Newtonian fluid flows.

The remainder of this paper is organized as follows: the next section describes the experimental setup and the instrumentation used. This is followed by the presentation and discussion of the experimental results inside the rectangular duct and in the impinging flow cell. Then, we present some results of numerical simulations after a brief description of the governing equations, the numerical method and the validation procedure. In the sequence, we present the flow pattern in the cell, the three-dimensional effects and finally a parametric study regarding the recirculation length. The paper closes with a summary of the main conclusions and an outline of future work.

2. Experimental rig and instrumentation

2.1. Experimental set-up

The flow loop used in the present experiments is shown schematically in Fig. 1. In the following description, we refer to numbers in parentheses identifying rig components, as in the figure. Flow was provided by a progressive cavity pump (2) (mono pumps Dresser model CB081AC1A3/G) fed directly from a stainless steel tank of 175 l of capacity (1). One pulsation damper (3), located immediately downstream of the mono pump outlet, was used to smooth out the flow and to remove any pulsations prior to the inlet of the entrance reservoir (5). At the top of this reservoir, an air chamber dampened any residual pulsations in order to ensure a steady flow at the rectangular duct inlet. The 2.6 m long rectangular duct (6) was made of four modules and had an internal cross section area of 0.0052 m^2 (height (H) x width ($2*W$) = 0.02 m × 0.26 m, corresponding to an aspect ratio (AR) of 13). Each module was constructed from stainless steel plates, machined and ground to size and then assembled with screws and a bonding agent. Visual inspection did not show any misalignment or a step that could perturb the flow.

The origin of the coordinate system is located right in the middle of the rectangular duct exit cross section; with x denoting the streamwise coordinate in the duct, y the transverse coordinate and z the spanwise coordinate. This coordinate system is drawn in Fig. 2, where the cell test section (7) is schematically represented. The test section has two inclined plane walls, each one making an angle of
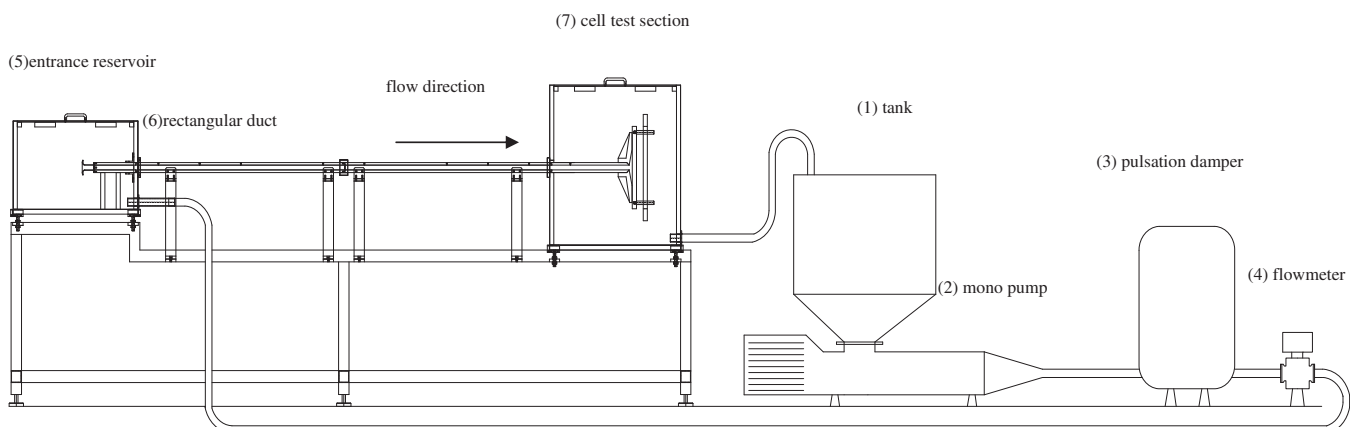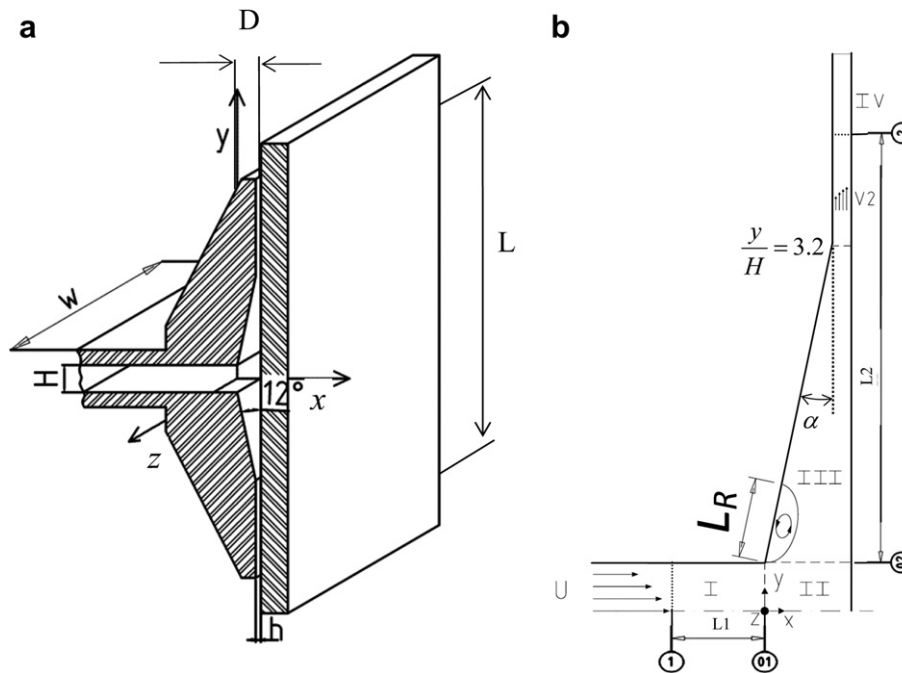

Fig. 1. Schematic representation of the flow loop.

Fig. 2. Schematic representation of the cell test section and coordinate system centered in the *x*-*y* and *x*-*z* symmetry planes; a) only half the cell test section is shown; b) A quarter of the cell is shown (the Roman numbers refer to the blocks of the computational meshes).

12° relative to the flat surface (impinging plate), in order to confine the jet flow inside the cell.

The fluid exits the test section through two symmetric thin vertical channels, each 4 mm thick (h) and having the same width as the inlet rectangular duct, thus defining an aspect ratio of 65 for the identical outlet channels. The reservoirs (5) and (7) and the cell were made of acrylic to allow velocity measurements using a laser Doppler anemometer (LDA).

Eleven pressure taps were drilled along the rectangular duct *x*-*y* center plane, with 200 mm spacing between consecutive taps. They were used to study the development of the flow along the duct and in addition they did not show any signs of misalignment between the duct modules (manufactured to within machine tolerances of ±10 μm), i.e., from visual inspection of the rectangular duct and from the pressure drop measurements and LDA measurements we did not observe any detectable perturbation to the flow.

Pressure differences were measured by a differential pressure transducer, model P305D-S20 from Valydine. The transducer calibration was carried out in a device made up of two independent water columns with the water level checked by two precision rules with accuracy better than 0.1 mm. All the pressure taps were drilled carefully to avoid spurious edge effects. For the design of pressure taps, recommendations from the literature were followed [9,32].

An electromagnetic flowmeter, type Mag Master (4) from ABB Taylor, measured the volumetric flow rates ($\dot{Q}_{in}$) in the range of 0–5 l/s with an accuracy of 0.2% of full scale.

All the instruments were connected to a 486 PC provided with a data acquisition board interfaced with an Advantech PCLD-8115 card.

2.2. Laser-Doppler system and fluids

A 1-D LDA from Dantec was used to measure the mean and root-mean-square velocity fields. The LDA was used in the forward scatter mode and the light source was an air-cooled, multimode 300 mW Ar-ion laser. The beam passed through a series of optical elements before the Bragg cell, where a frequency shift of 0.6 MHz was imposed. The front lens had a 300 mm focal length and the scattered light was collected by a photo-multiplier before which stood an interference filter of 514.5 nm. After being band-pass filtered, the signal from the photo-multiplier was processed by a TSI 1990C counter operating in the single measurement per burst mode with a frequency validation setting of 1% in the 10/16 cycle comparison. A 1400 Dostek card interfaced the counter with an 80486 based computer to provide all the statistical quantities via a purpose-built software. For each point measured, a sample size of 10,000 values was taken. The refraction of the laser beams at the plane walls of the duct and of the cell was taken into account to correct the position of the control volume. Table 1 provides the main characteristics of the LDA control volume.

The LDA probe was mounted on a milling table with movement in the three spatial coordinates. The system was used to measure both the mean and fluctuating velocities in the horizontal (u) and vertical (v) directions along the rectangular duct and inside the cell. For the horizontal velocity component inside the rectangular duct the laser beams were set to cross each other in a horizontal plane and measurements could be performed well close to the lower and upper channel walls.

When measuring inside the cell, the horizontal velocity component (u) could not be measured directly near the inclined wall, because one of the beams collided with the wall. In such cases the u velocity component was determined using trigonometry and

Table 1
Main characteristics of the LDA in air at e^{-2} intensity.

Laser wavelength	514.5 nm
Measured half angle of beams in air	3.65°
Dimensions of the measuring volume in air:	
Major axis	2.53 mm
Minor axis	146 μm
Fringe spacing	4.041 μm
Frequency shift	0.6 MHz

from measurements of the vertical velocity component (v) and of a velocity component at an angle of 24° relative to the vertical direction. Due to optical access limitations, these velocity measurements inside the cell were not performed at the x- y center-plane, but at a plane $z/W = 0.45$ halfway between the center-plane and the side wall, where the effect of the side wall on the flow was still negligible, as will be shown in Section 3. Typical uncertainties associated to the measurement of the mean and fluctuating streamwise velocity data were estimated to be 1% and 4%, respectively. These increased to 2% and 5% for transverse mean and fluctuating velocities and to 3.5% and 14% for the indirectly measured mean and fluctuating horizontal velocities inside the cell, respectively.

A single fluid was used, a glycerol-water mixture at 25 °C with density and dynamic viscosity of 1184 kg/m^3 and 0.0425 Pa s, respectively. The shear viscosity was measured with a rheometer from Physica, model MCR 301, using the low viscosity double-gap concentric cylinder system, which allowed the measurement of viscosities between 1 mPa s and 67.4 mPa s, at a maximum shear rate of 4031 s^{-1}. A thermostatic bath and a temperature control system, Viscotherm VT, allowed the control of the temperature of the fluid sample to be within ±0.1 °C.

3. Experimental results

3.1. Fully-developed flow in the rectangular duct

Transverse profiles of streamwise velocity were measured along the rectangular duct and compared with data from the literature, in particular for fully-developed flow. The flow Reynolds numbers are $Re = 136$ and $Re = 275$ based on the hydraulic diameter of the rectangular duct and on the bulk velocity, U, calculated from the measured flow rate. The velocity data were normalized by the mean velocity at the rectangular channel, the x and y coordinates by the height of the duct (H) and the z coordinate by the half-width of the channel (W). The laminar flow data are compared at times with turbulent flow data measured by Cavadas [2] in the same geometry at a Reynolds number of 13750.

In Fig. 3, the measured profiles of streamwise mean velocity are shown at $x/H = -5.7$, a plane where the flow is already fully-developed, and corresponding to a distance of 124.3 channel heights downstream of the duct inlet. The measured data are also compared with the theoretical expressions for the rectangular duct flow ($AR = 13$) [39], and for the parallel plate flow ($AR = \infty$). The two theoretical curves differ by 3% and the experimental profile

differs from any of them by around 1%, i.e., within experimental uncertainty. The filled symbols represent the reflected profile from one half of the duct to the other half and allow a better assessment of flow symmetry. The flow is symmetric relative to the $y/H = 0$ center-plane. The symmetry in relation to the $z/W = 0$ center-plane can be assessed by inspection of Fig. 4, where the corresponding spanwise profiles of the streamwise velocities are plotted. The flow is again symmetric and the presence of the end walls is not felt in the region $-0.6 \leq z/W \leq +0.6$. This also justifies the measurements of velocity inside the cell at $z/W = 0.45$ as representative of the behavior at the center-plane ($z/W = 0$), as mentioned in Section 2.2. Measuring closer to the side wall reduces the optical limitations, but it is necessary to ensure that the data are not affected by side wall effects.

The pressure drop measurements along the $z/W = 0$ center-plane resulted in a friction factor of 0.67 at a Reynolds number of 136, in close agreement with the value of 0.65 in [39]. In the laminar regime, the development length is about $L/D_H \approx 0.067Re$ which corresponds to $L/D_H = 9.1$ and 18.4 for $Re = 136$ and 275, respectively. The location $x/H = -5.7$ corresponds to a length of 64.3 measured from the beginning of the duct.

Hence, based on the velocity and pressure measurements inside and along the rectangular duct it was concluded that the flow was fully developed upstream of the cell test section for the investigated conditions.

3.2. Approach flow and impinging flow region

The general behavior in the approach and impinging regions for jets with small nozzle to plate distances has been well documented in the literature [3–6] but concerning different geometries and/or fluids, like multiple impinging jets with confinement by a parallel plate with Newtonian or inelastic non-Newtonian fluids of variable viscosity.

In spite of the large inertial forces involved, the impinging plate clearance is sufficiently small to affect the rectangular duct flow inside the final part of the duct as it approaches the exit. The upstream vorticity diffusion created by the impinging plate is responsible for this perturbation as is typical of other flows with entrance effects [35,37]. This effect is shown in the streamwise evolution of the streamwise velocity in Fig. 5. Here, we plot the transverse profiles of u at $z/W = 0$ center-plane at different streamwise locations. The first profile corresponds to the fully-
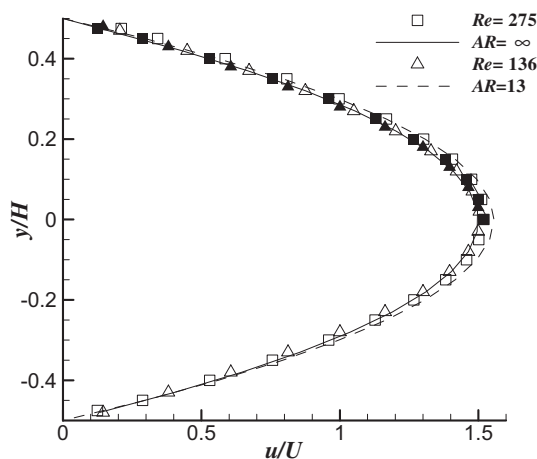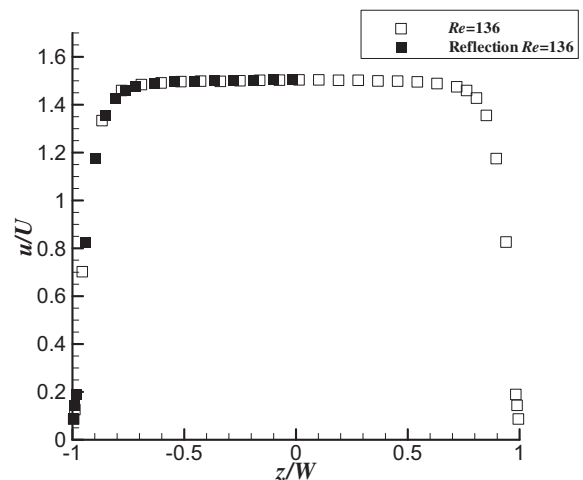

Fig. 3. Transverse profiles at $z/W = 0$ of the mean streamwise velocity for fully-developed rectangular duct flow at $x/H = -5.7$ and $Re = 136$ and 275.

Fig. 4. Spanwise profiles at $y/H = 0$ of the mean streamwise velocity for fully-developed rectangular duct flow at $x/H = -5.7$ and $Re = 136$ (closed symbols refer to the reflected profiles).
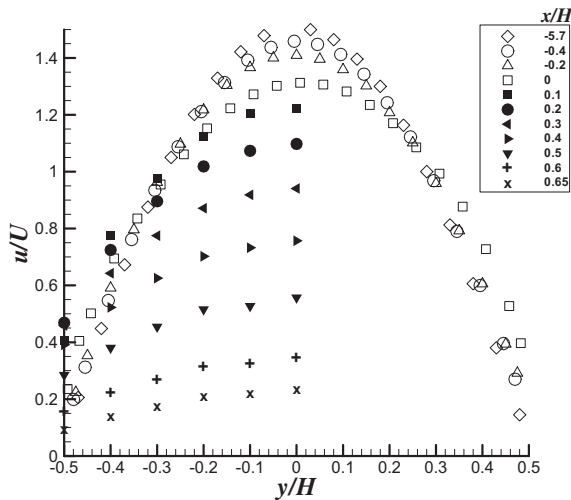
Fig. 5. Variation of the streamwise mean velocity in the approach flow region for $Re = 136$ and $z/W = 0$; transverse profiles of streamwise velocity at the end of the duct and in the impact region.

Fig. 6. Variation of the streamwise mean velocity in the approach flow region for $Re = 13,750$ [2] and $Re = 136$ at $z/W = 0$; streamwise velocity profile along the cell axis.

developed flow inside the rectangular duct and is identical to that shown in the previous section. Even though the flow is laminar, the influence of the impinging plate is essentially identical to that observed by Cavadas [2] in the turbulent regime, at $Re = 13750$, with a small effect of deceleration in the location $x/H = -0.4$. At this location for the laminar flow, the effect of the plate is still rather weak, with values of velocity differing from the fully-developed profile by less than 2.5%. As for the turbulent flow, when $x \rightarrow 0$, there is a progressively lower streamwise velocity in the center of the duct, whereas, near the wall, the velocity and its transverse gradient increase. All profiles in Fig. 5 exhibit symmetry relative to $y/H = 0$ center-plane. We can also see that after the end of the rectangular duct, the velocity decreases considerably and the velocity profile becomes more uniform as the jet approaches the impinging plate. At $x/H = 0.65$, the profile is almost uniform, but not as much it was in the turbulent flow data of [2].

In Fig. 6, we represent the variation of the streamwise velocity along the cell axis (u_c) in the region $-0.4 \leq x/H \leq 0.8$, i.e., at the end of the rectangular duct ($x < 0$) as well as in the impinging region above the plate ($x > 0$). The figure includes data for the turbulent regime. The velocity has been normalised by the corresponding fully-developed value (U_0). The decrease of u_c/U_0 inside the duct is only by about 10% and the strong flow deceleration actually takes place in the vicinity of the impinging plate ($0.2 \leq x/H \leq 0.8$). From the figure, we can see also that the velocity decrease near the impinging plate is quicker in the laminar regime than in turbulent flow, as expected on account of the stronger inertia of the latter, which, as a consequence, will have a stronger reduction to zero very close to the plate.

The variation of the streamwise dimensionless strain rate

$$\dot{\varepsilon}^* = \frac{\partial u}{\partial x} \frac{D_H}{U_0} \qquad (1)$$

as well as the variation of the dimensionless streamwise advective acceleration

$$a^* = u \frac{\partial u}{\partial x} \frac{D_H}{U_0^2} \qquad (2)$$

are both plotted in Fig. 7 for $Re = 136$ and $Re = 13,750$.

The values are negative, meaning deceleration, and the strongest deceleration is found between $0 \leq x/H \leq 0.5$, with the peak
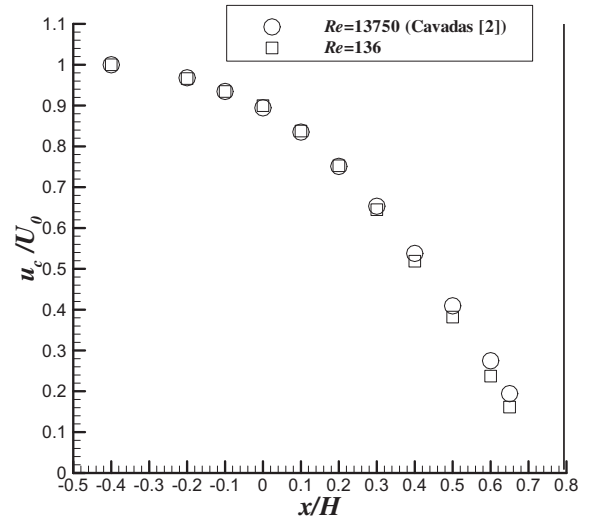
value at $x/H = 0.3$ for both Reynolds numbers, with the deceleration being slightly higher for $Re = 136$. As the fluid further approaches the plate, the deceleration must drop to zero since the plate is impermeable (cf. Fig. 2). In contrast, the velocity gradient varies differently and keeps increasing (in magnitude) reaching the highest value at around $x/H = 0.6$ for $Re = 136$ and being higher for the case of turbulent regime ($Re = 13,750$). Note that due to blockage of the laser beams by the solid walls, we could not measure closer to the impinging plate so that the values plotted in Fig. 7 at $x/H \approx 0.8$ are theoretical.

Velocity peaks of the impinging jet flow have been observed by Sezai and Mohamad [33] to occur simultaneously off-center and off-stagnation for laminar rectangular single jet flows with small jet to wall distances. The formation of these velocity peaks near the edges of the jet is generally attributed to fluid deceleration and continuity requirements [16,36,38]. On the other hand Chatterjee and Deviprasath [5], attribute the formation of off-center off-stagnation velocity peaks to the distortion in the velocity distribution at the jet exit plane as a result of diffusion of vorticity, which is generated at the impingement surface. However, in the present study, no off-center and off-stagnation velocity peaks were observed. The inclination of the confined walls and the quasi-
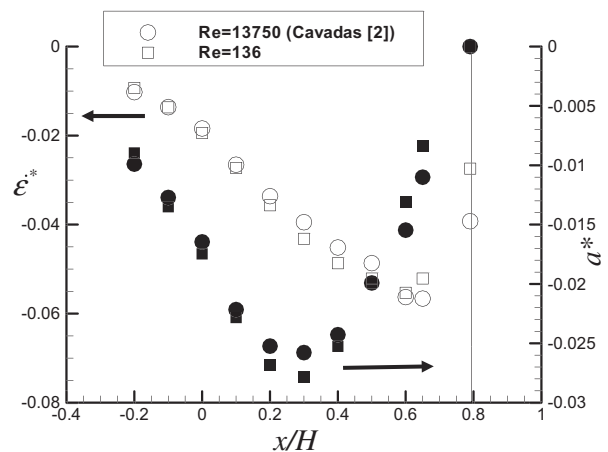

Fig. 7. Variation of the x- component rate of strain ($\dot{\varepsilon}^*$) and acceleration profiles (a^* - full symbols) in the symmetry plane $z/W = 0$ for $Re = 13,750$ [2] and $Re = 136$.

parabolic velocity profile emerging from the jet nozzle are responsible for the absence of this peak. The wall inclination retards the flow deceleration in the y-direction just after the nozzle and induces a recirculation region, which will be discussed in the next section. The shape and dimensions of this separated flow region are such that while enforcing continuity the fluid continuously accelerates in the y direction from the $y/H = 0$ center plane toward the cell exit.

3.3. Flow within the cell

The flow symmetry inside the test cell is shown in Figs. 8 and 9, relative to the $z/W = 0$ and $y/H = 0$ planes, respectively. The spanwise profiles of streamwise velocity (now the v component) plotted in Fig. 8 show the symmetry in the spanwise direction, where the closed symbols are the reflection of the velocity profile from one half of the duct onto the other half. These profiles were measured at $x/H = 0.45$ and $y/H = -0.6$, and at $x/H = 0.525$ and $y/H = -1.65$, but a similar behavior (not shown) was observed at other locations. The flow visualization performed with dyes confirmed the flow symmetry inside the cell.

Fig. 9 assesses the flow symmetry relative to the $y/H = 0$ centerplane, in this case where the main flow divides into two streams after impinging the plate, showing the transverse profiles of the v-velocity component in the upper and lower exit rectangular channels (for the lower channel we plotted -v). The velocity profiles were not taken at $z/W = 0$, but at $z/W = 0.45$ in order to reduce the blockage of the laser beams. As discussed above, this plane is inside the region $-0.6 \leq z/W \leq +0.6$ where the streamwise velocity is essentially constant and unaffected by the end walls, as shown in Section 4.1. The two profiles are normalized by the mean velocity at the inlet duct and the differences between them do not exceed 4%, a good value taking into account the uncertainty of ± 0.2 mm associated with the 4 mm thickness of the exit channels. This thickness of 4 mm is adjusted with four screws separating the impinging plate and the block containing the inclined walls and a minor misplacement can easily lead to a flow rate separation different from the desired 50%–50% flow rate separation. That is not the case here, with the flow dividing symmetrically (within 4%) into the two cells.

Fig. 10 (a) presents a streamline contour plot for $Re = 136$ where no flow separation is observed in contrast with the turbulent flow
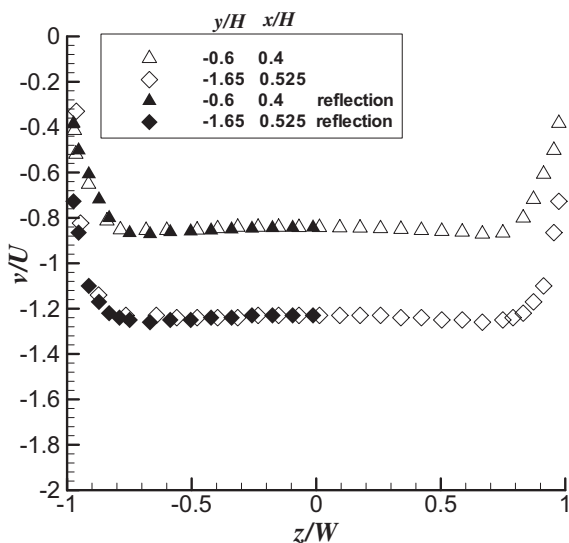

Fig. 8. Profiles of streamwise velocity inside the cell for $Re = 136$; spanwise profiles at $y/H = -0.6$, $x/H = 0.45$ and $y/H = -1.65$ $x/H = 0.525$ (closed symbols refer to the reflected profiles).
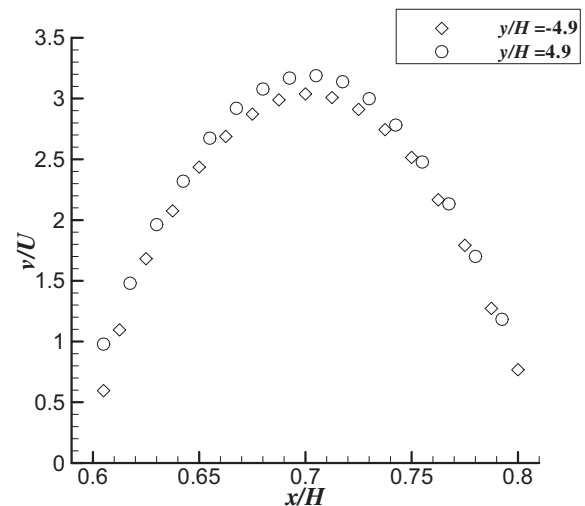

Fig. 9. Profiles of streamwise velocity component inside the cell for $Re = 136$; transverse profiles at $z/W = 0.45$ for O $y/H = 4.9$ and $\Delta y/H = -4.9$ (-v/U is plotted at $y/H = -4.9$).

case of Cavadas [2] and with the laminar flow at $Re = 275$ shown in Fig. 10(b). Strictly speaking there are no streamlines in a 3D flow, so here these lines are computed as if the flow was 2D.

Meanwhile, the flow visualizations showed that for a Reynolds number higher than 208, a separation zone becomes visible in the central plane. The plot of Fig. 10(b) corresponds to this flow condition and shows a recirculation zone with a normalized length $L_R/H = 0.35$ measured along the inclined wall and obtained from the detailed LDA velocity measurements. The normalized profiles of streamwise velocity plotted in Fig. 11 correspond to the same two laminar flow cases and were taken downstream of the recirculation for $Re = 275$. For $Re = 275$, the velocity near the inclined wall is lower than for $Re = 136$, because of the presence of the recirculation zone. In both cases, the flow accelerates along the flat wall because inertia pushes the fluid toward this plane, an effect that is enhanced by the presence of the separated flow region, hence explaining the higher velocities for $Re = 275$. The narrowing channel also enhances the role of inertia, but this effect is present at both $Re = 136$ and 275.

In this part of the cell, there is now a three-dimensional flow, while in the turbulent regime there was already a three-dimensional flow in the approach flow (cf. Cavadas [2]). However, the causes for these two three-dimensional flow features are different. In turbulent flow, the three-dimensional features of the approach flow were associated with gradients of normal Reynolds stresses [18], whereas the three-dimensional laminar flow within the cell is a consequence of the interaction between the side wall and the separated flow.

In the laminar flow inside a conical cell of Miranda and Campos [19], the above mentioned three-dimensional flow inside the cell is absent due to axisymmetry, but there was a second separated flow region downstream of the first recirculation and attached to the impinging plate. This second recirculation tended to become unstable as the flow rate was increased. Here, we do not find this second recirculation attached to the impinging plate.

3.4. Three-dimensional effect

The fluid exiting the rectangular duct is forced to turn around a sharp corner by 90° and to go into the cell. At a Reynolds number above 208, the flow separates at the corner and reattaches downstream, but near the side walls the separated flow region does not
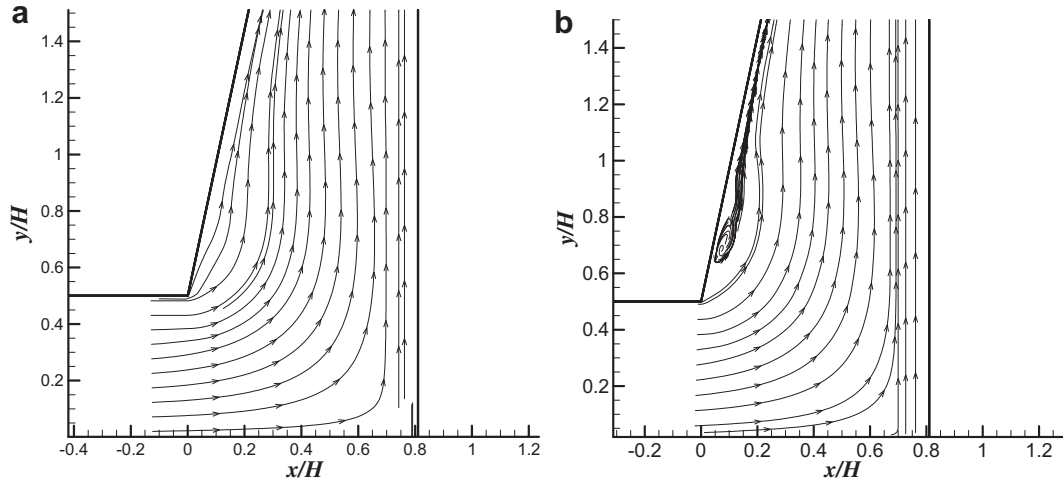
Fig. 10. Flow characteristics inside the cell; Streamlines contour plot of the u and v-velocity components at z/W = 0.45; (a) Re = 136; (b) Re = 275.

exist. The different flow characteristics near and away from the side walls creates a spanwise pressure gradient that is responsible for a swirling secondary flow and a near wall jet, which we denote as the characteristic three-dimensional effect discussed below.

Fig. 12 shows some spanwise profiles of the vertical mean velocity, measured inside the lower half of the cell test section (negative velocities),pertaining to both laminar Reynolds numbers. At Re = 136 the absence of a separated flow region minimizes any spanwise pressure gradient and any velocity in this direction, so no flow jet is observed near the side wall, consequently the stream-wise velocity naturally drops to zero as we approach the side wall. However, at Re = 275, a small wall jet can be seen very close to the wall in the velocity profile at y/H = -1.65 and x/H = 0.525 for z/W ≈ 0.95. Closer to the wall, we do not see the velocity decreasing to zero, because here this variation is very steep and occurs across

the largest dimension of the LDA control volume (cf. Table 1), i.e., there is here a large bias effect and the LDA control volume enters the wall as we try to measure close to it. The profiles of y-velocity at Re = 275 also show that near the side wall, there is no separated flow, as already mentioned.

Flow visualizations with a dye injection technique and with small tracer bubbles, have shown the existence of a helical flow motion inside this recirculation as sketched in Fig. 13a). Fluid particles entering the separated flow region rotate away from the center, flowing toward the side walls, where they exit, merging with the main flow, and thus creating a vertical side-wall jet. The three-dimensional calculations confirmed the experimental observations, as seen in the streakline plot of Fig. 13b) at Re = 275, drawn from the numerical results that will be presented in the following section. The streaklines drawn for Re = 275 show the three-dimensional nature of the flow inside the separated flow region, which consists of a helical fluid motion along the spanwise direction from the center of the cell toward the flat walls. Before reaching the side walls, the fluid in helical motion exits the separated flow region and joins the main flow creating a jet near the side wall, but still close to the inclined plate. Away from the inclined plate, the fluid that exits the rectangular inlet channel near the side wall turns into the vertical channel swirling as shown in the streakline plot of Fig. 14. Therefore, the oscillations in the velocity profiles seen in Fig. 12(b) at y/H = 1.65 and x/H = 0.525 and the consequent velocity peaks near the side wall are the result of a complex interaction between this side wall, the flow exiting the separated flow region and the swirling motion of the main fluid stream.

4. Numerical investigation of the flow in the cell

Numerical calculations of this laminar flow were carried out with an in-house code and were aimed at investigating the flow characteristics inside the cell test section and their dependence on Reynolds number and inlet geometry. Next we present the gov-erning equations and briefly describe the numerical method.

4.1. Governing equations

The governing equations were those for three-dimensional, incompressible and isothermal laminar flow of constant density Newtonian fluids, written below in Cartesian index notation. They are the continuity equation:
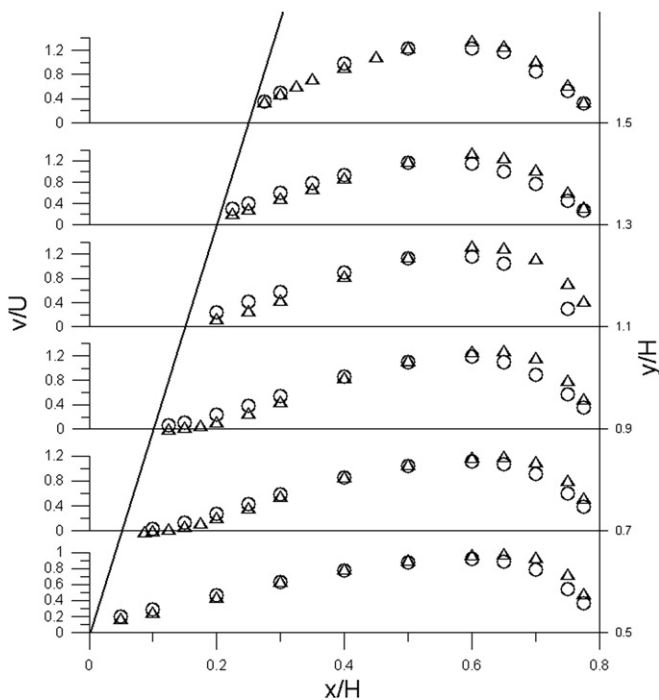

Fig. 11. Transverse profiles of mean vertical velocity inside the cell at z/W = 0.45, for (O) Re = 136 and (△) Re = 275.
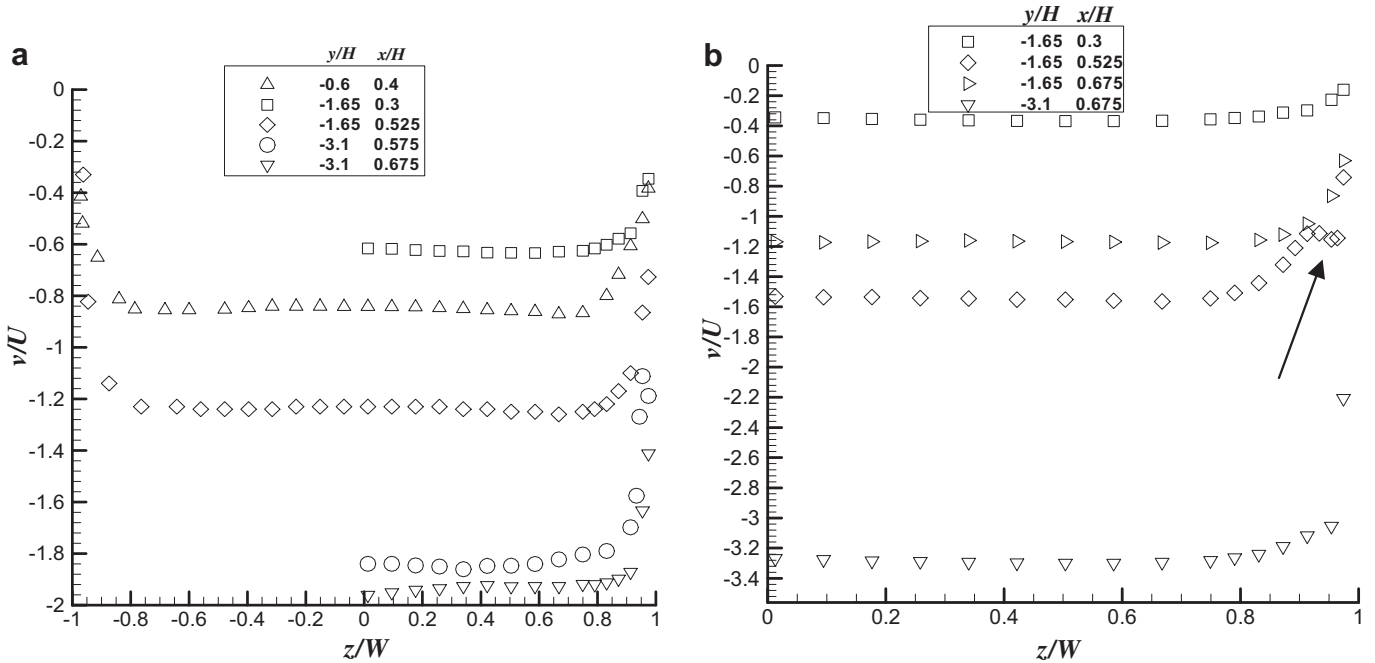
Fig. 12. Three dimensional flow effect near the side walls; Spanwise profiles of streamwise velocity at various locations: (a) $Re = 136$ (b) $Re = 275$.

$$\frac{\partial u_i}{\partial x_i} = 0 \tag{3}$$

and the transport equation of linear momentum :

$$\frac{\partial \rho u_i}{\partial t} + \frac{\partial \rho u_j u_i}{\partial x_j} = -\frac{\partial p}{\partial x_i} + \frac{\partial}{\partial x_j}\left(\eta \frac{\partial u_i}{\partial x_j}\right) \tag{4}$$

where u_i is the velocity vector component along the Cartesian coordinate x_i, ρ is the fluid density, p the pressure and η is the viscosity coefficient. These equations allow the determination of the velocity and pressure flow fields. A fully-implicit finite-volume method was used to solve Equations (3)–(4), as described below.

4.2. Numerical procedure and validation

The numerical method is briefly outlined below, since it is described in detail in the literature (cf. Oliveira et al. [24]. The numerical simulations were carried out with a finite-volume method using non-orthogonal collocated grids and second order accurate differencing schemes to discretize all terms of the transport equations [27] and [28]. The main code is interfaced with a mesh generation pre-processor and adequate data post-processor, as described in Oliveira [24]. The basic differencing schemes were central differences for the diffusion terms and a high-resolution method, CUBISTA described in Alves et al. [1], for the convective terms. The solution algorithm was a modified version of the SIMPLEC algorithm of van Doormal and Raithby [34]
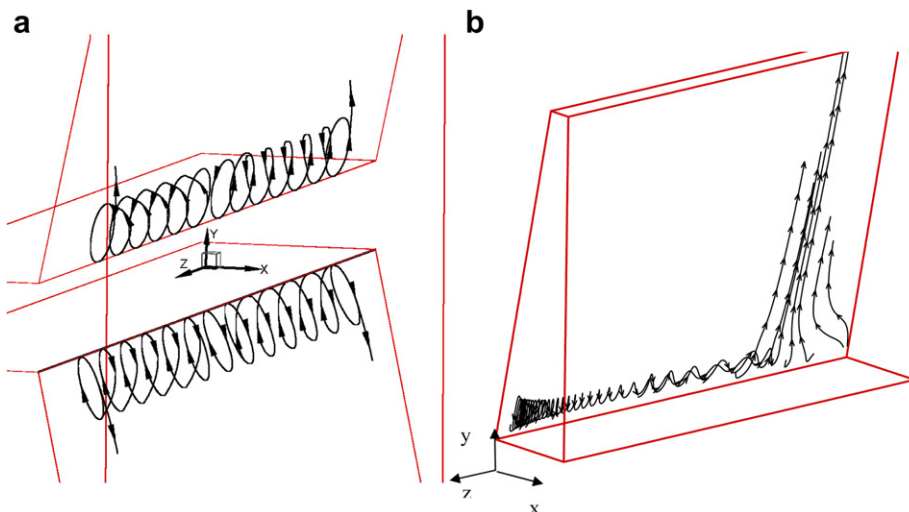

Fig. 13. Three dimensional flow effect near the side walls: a) sketch of the flow in the separated flow region; b) Streamtraces in the recirculation zone for $Re = 275$ (for a quarter of the cell).
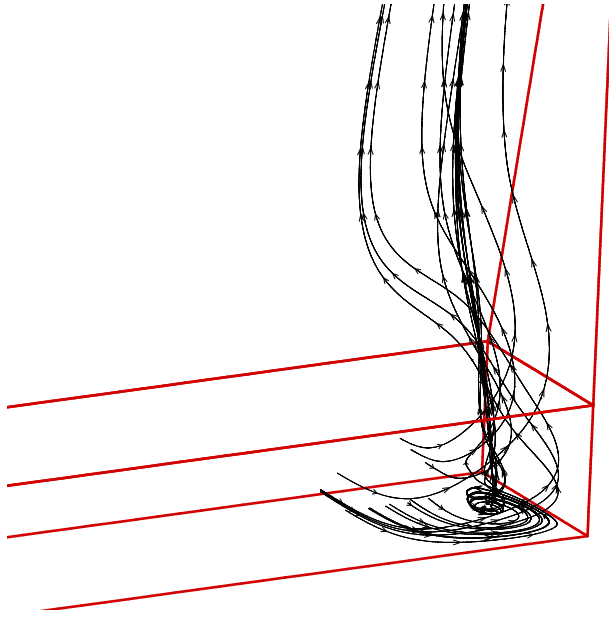
Fig. 14. Flow streaklines within the cell for $Re = 275$, $h = 4$ mm, starting at the exit of the inlet duct ($x/H \approx 0$) and near the side wall.

adapted for time marching as explained in Issa and Oliveira [13], where details to evaluate mass fluxes at cell faces are given.

As shown by the experimental results, the flow symmetry relative to the $z/W = 0$ and $y/H = 0$ center planes allowed us to reduce the computational domain to a quarter of the physical domain. On the center planes, symmetry conditions were assumed, and at the wall, all velocity components were set to zero. At the inlet of the rectangular duct, the flow profile was set to uniform with the flow developing along the duct.

The computational grids were generated using patched blocks, one for the inlet of the channel, two for the cell zone, and one for the outlet of the channel, as schematically shown in Fig. 2(b). The length of the computational inlet and outlet channels used, L_1 and L_2, were 2,6 m and 0.48 m, respectively. Details of the meshes are given in Table 2, listing the number of internal cells in the three directions (Nx,Ny,Nz) and the corresponding geometric expansion (or contraction) factors for mesh spacing (fx,fy,fz). The mesh spacing

was non-uniform, with mesh points concentrated in the cell zone. The expansion factors used were carefully chosen to guarantee a smooth variation in size between consecutive cells in the whole domain, and in particular at the interfaces between the mesh-generating blocks. Several tests with different grids were initially performed to assess the adequacy of the computational domain, of the mesh used as well as of the degree of grid refinement required for grid-independent results.

In the grid tests, we analyze the behavior of the length of the separated flow region along the inclined walls (L_R/H) (c.f. Fig. 2(b)). This recirculation length varies along the spanwise direction as shown in Fig. 15 for different meshes. Grid M40 is the finest, leading to just under 4 million degrees of freedom, but it has a large computational cost. Consequently, most simulations were carried out using grid M30a), even though there is a 5% difference in L_R/H at the symmetry plane ($z/W = 0$) relative to the value predicted by grid M40. Nevertheless, the agreement with experimental data is good as shown below, and we should emphasize that grid M30a) is actually finer than grid M40 in the spanwise direction in order to better resolve variations along z.

We end this section with comparisons between the numerical predictions and the experimental data for Newtonian fluids at $Re = 136$ and $Re = 275$, for the purpose of validation including theory when available. We start by comparing in Fig. 16 (a) transverse profiles of streamwise velocity for fully-developed laminar flow in the rectangular duct. In addition to the experimental data, the plot includes the analytical solutions for this channel ($AR = 13$) and for an infinite channel ($AR = \infty$), given by White [39].

The numerical simulations obtained with grid M30a) are in very good agreement with the theoretical solution and differ by 5% from the experimental data. Fig. 16(b) compares experimental and numerical velocity data at the impinging jet region, via transverse profiles of streamwise velocity at $y/H = 0.8$ and $z/W = 0.45$ for $Re = 136$ and $Re = 275$. Here, the flow is decelerating fast and the predictions agree very well with the measured data.

To finish the validation, spanwise profiles of streamwise velocity at $y/H = 1.65$, $x/H = 0.525$ located inside the cell (see inset) are compared in Fig. 17. Again, the agreement between predictions and experiments is very good and the maximum difference between numerical and experimental data does not exceed 5%. Note that in this region, the duct is narrow and the velocity profiles are very sensitive to uncertainties in the channel width. The predicted velocity profiles have the same shape as the experimental profiles,

Table 2
Characteristics of the numerical meshes.

Grid	Block1			Block2		
	Nx/fx	Ny/fy	Nz/fz	Nx/fx	Ny/fy	Nz/fz
M15	50/0.8926	15/1	15/1.0494	20/1	15/1	15/1.0494
M20	67/0.9183	20/1	20/1.03683	26/1	20/1	20/1.03683
M20 a)	67/0.9183	20/1	120/1.0061	26/1	20/1	120/1.0061
M30	100/0.9448	30/1	30/1.0244	39/1	30/1	30/1.0244
M30 a)	100/0.9448	30/1	60/1.01213	39/1	30/1	60/1.01213
M30 b)	100/0.9448	30/1	70/1.0104	39/1	30/1	70/1.0104
M40	133/0.9583	40/1	40/1.0183	52/1	40/1	40/1.0183

| Grid	Block3			Block4			Total n. of cells
	Nx/fx	Ny/fy	Nz/fz	Nx/fx	Ny/fy	Nz/fz	
M15	20/1	88/1.0005	15/1.0494	20/1	38/1.0736	15/1.0494	53550
M20	26/1	117/1.0004	20/1.03683	26/1	50/1.0547	20/1.03683	124040
M20 a)	26/1	117/1.0004	120/1.0061	26/1	50/1.0547	120/1.0061	744240
M30	39/1	175/1.0003	30/1.0244	39/1	75/1.0003	30/1.0244	417600
M30 a)	39/1	175/1.0003	60/1.01213	39/1	75/1.0003	60/1.01213	835200
M30 b)	39/1	175/1.0003	70/1.0104	39/1	75/1.0003	70/1.0104	974400
M40	52/1	233/1.0002	40/1.0183	52/1	100/1.0183	40/1.0183	988640
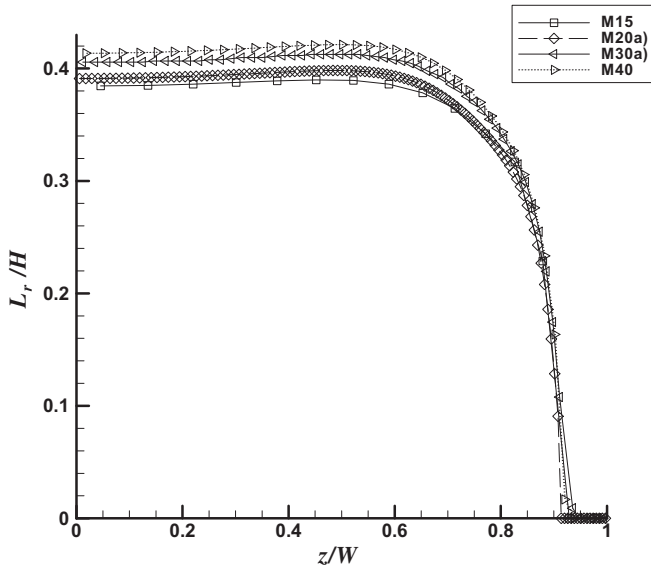
Fig. 15. Spanwise variation of the length of recirculation at $Re = 275$ for different meshes.

with two velocity peaks appearing near the walls. These velocity peaks belong to the near side-wall jets resulting from the merger of the secondary spiraling flow coming from within the separated flow region with the main flow coming from the rectangular duct, as already discussed in section 3.4.

4.3. Recirculation length and flow pattern in the cell

In this section, we investigate numerically and in detail the effects of the Reynolds number, of the thickness of the exit channel and of the sloping plane angle, on the flow characteristics inside the cell test section.

Fig. 18 shows the variation of the recirculation length (L_R/H) with the spanwise coordinate (z/W) as a function of Reynolds number for a constant exit channel thickness (h) of 4 mm ($D/H = 0.786$ where D represents the distance from the exit of the rectangular duct to the impinging plate, see Fig. 2); note that $h = 4$ mm corresponds to the experiments. L_R is constant over most of the channel, decreasing to zero on approaching the side walls, i.e., the flow is never separated in the 10% closer to the side walls, regardless of the Reynolds number. With increasing Reynolds number, the width of the constant L_R/H region is also reduced suggesting the strong coupling between 3D effects and inertia: for $Re = 136$ the central region occupies 70% of the channel span, decreasing to 50% at $Re = 1088$. It is interesting to notice also that the highest value of L_R/H is not at the center, but at the end of this central region, where L_R/H starts to decrease strongly. Although the difference between the maximum L_R/H and its plateau value is small, it is noticeable especially at large Reynolds numbers.

To assess the effect of h on L_R/H additional computations were performed for $h = 2$ mm ($D/H = 0.686$) and $h = 6$ mm ($D/H = 0.886$) and the corresponding spanwise variations of L_R/H as a function of the Reynolds number are plotted in Figs. 19 and 20, respectively. For a constant Reynolds number L_R/H increases with the thickness h and in all cases the separated flow region ends before the side wall is reached at around $z/W \approx 0.95$ regardless of the Reynolds number and value of h. The width of the central region with near-constant L_R/H, is found to decrease with increasing thickness h.

The variation of L_R/H with h for a constant inclination of the confining plane is easy to understand. The decrease of h reduces the thickness of the cell leading to an increased flow acceleration within the cell and, by consequence, to an increase in the flow kinetic energy along the plate. This correspondingly induces a strong and quick decrease of the flow pressure, which reduces the magnitude of any adverse pressure gradient within the cell and the separated flow region becomes shorter. It is interesting to note that the end of the separation zone in the spanwise direction at $z/W \approx 0.95$, is fairly independent of the Reynolds number and of the height of the duct.
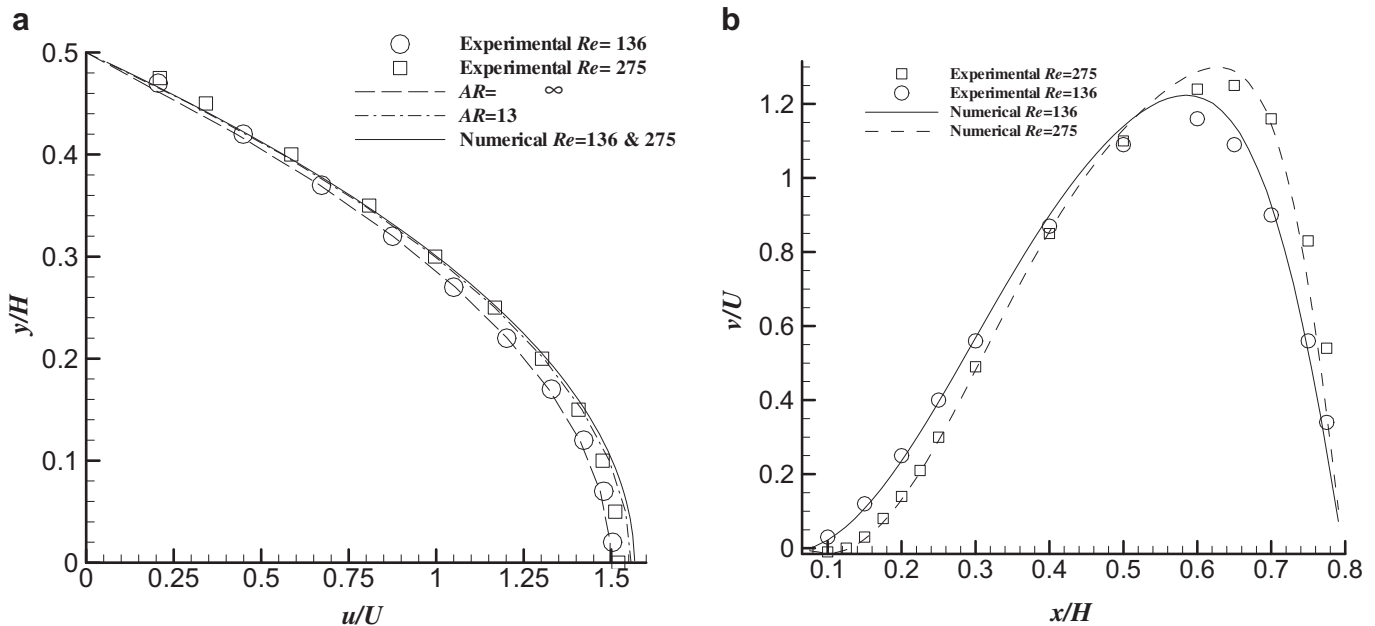

Fig. 16. Comparison between experimental (symbols), analytical (dashed lines) and numerical (solid line) data for laminar flow at $Re = 136$ and $Re = 275$: a) rectangular duct $x/H = -5.7$, $z/W = 0$; b) impingement region, $y/H = 0.8$, $z/W = 0.45$.
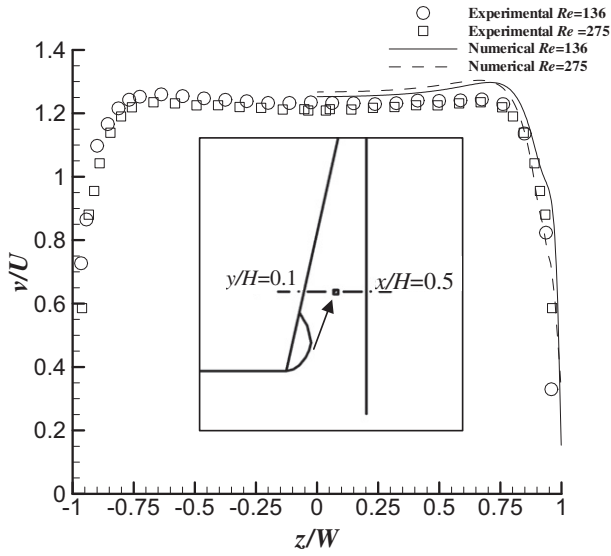
Fig. 17. Spanwise profiles of streamwise velocity (within the cell) for $Re = 136$, $Re = 275$, at $y/H = 1.65$ and $x/H = 0.525$.

To better understand why the longest recirculation length in the region $z/W = 0.6$ to 0.8 is found to decrease with increasing h, in Fig. 21 we plotted the contours of the normalized spanwise velocity component (w/U) at the plane $z/W = 0.77$, for the three exit channel thicknesses. This velocity component is characteristic of the secondary flow inside the separated flow region and it increases in magnitude as h decreases, thus feeding in fluid to the edge of the recirculation region hence helping to maintain a fairly constant L_R/H over most of the separated flow. This behavior of w is also observed at other constant z planes, but is not shown here for conciseness. Another immediate consequence of a larger w (stronger secondary flow) is an increase of the wavelength of the helical motion inside the separated flow region as h is reduced.

The effect of the angle of the sloping wall (α) was also investigated. Table 3 presents the recirculation length (L_R/H) at the $z/W = 0$ center plane as a function of Reynolds number, exit channel thickness and angle of the sloping wall and some of the
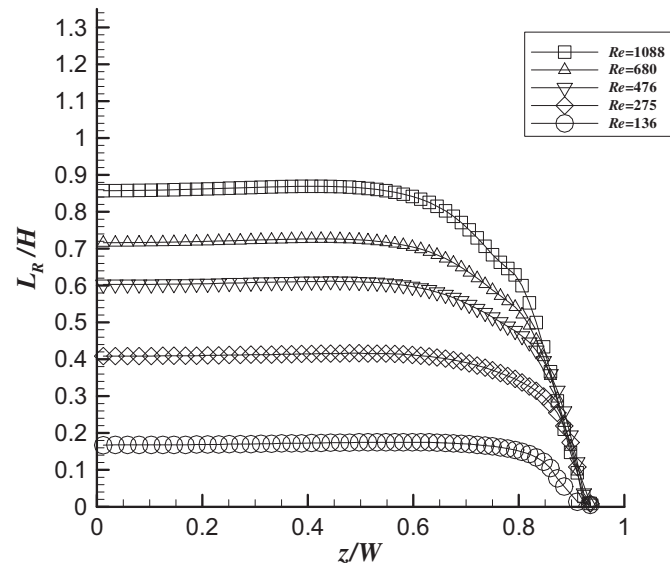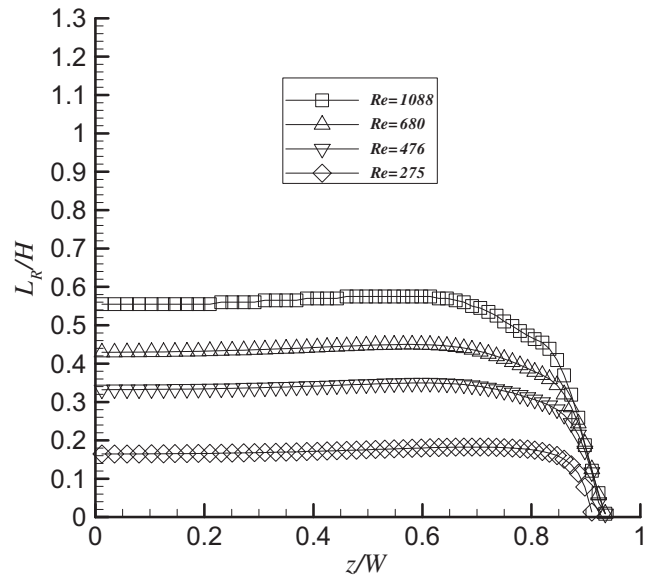

Fig. 19. Recirculation length (L_R/H) versus Reynolds number along the spanwise direction for $h = 2$ mm.

data are plotted also in Fig. 22. Fig. 22(a)) shows the variation of the shape of the separating streamline with Reynolds number for $h = 6$ mm ($D/H = 0.886$) and an angle of 30°, whereas Fig. 22(b) shows the variation of L_R/H with h and α for $Re = 1088$. Looking at Table 3 and these figures we observe that the separated flow region grows in length and width as the angle decreases and the Reynolds number and thickness h increase, all other parameters being equal. An increase in h and a reduction of α basically reduces the strength of the confinement within the cell and these tend to enhance flow deceleration thus facilitating flow separation.

4.4. Flow along the impinging plate

The numerical simulation results allowed studies of the shear stress and pressure variation along the impinging plate. In Fig. 23(a)
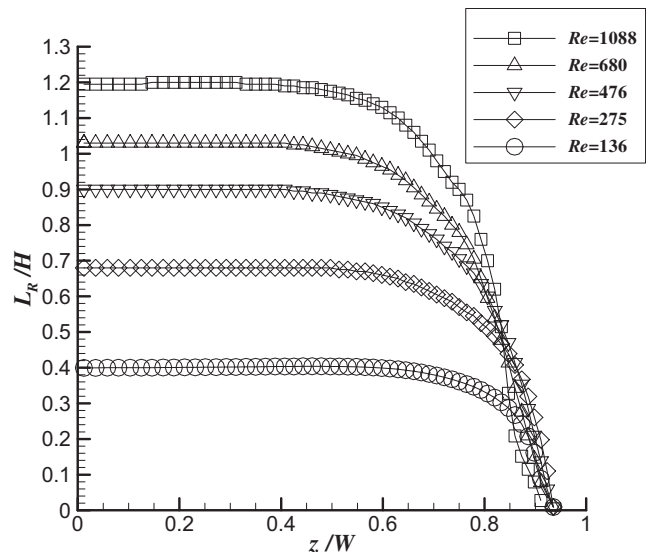

Fig. 18. Recirculation length (L_R/H) versus Reynolds number along the spanwise direction for $h = 4$ mm.

Fig. 20. Recirculation length (L_R/H) versus Reynolds number along the spanwise direction for $h = 6$ mm.
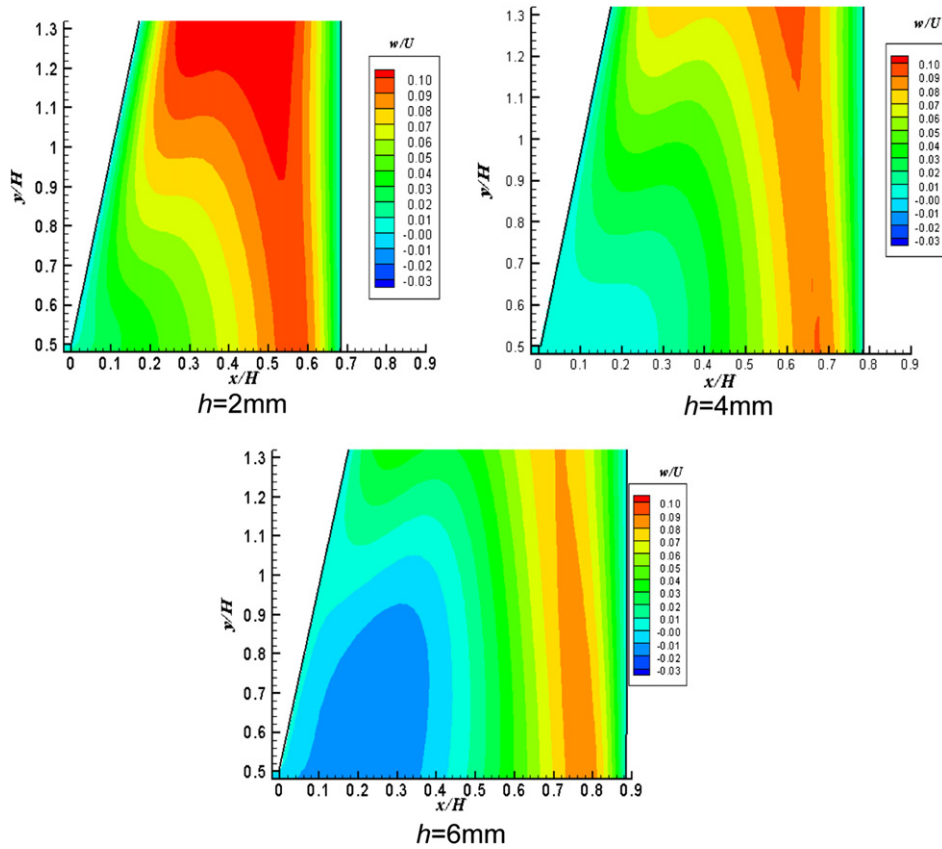
Fig. 21. Contours of the normalized spanwise velocity component (w/U) in plane $z/W = 0.77$ for the three exit heights ($h = 2, 4, 6$ mm).

and (b), contour plots of the normalised shear stress on the impinging plate and on the inclined wall are shown, respectively. The flow is from the bottom to the top, the coordinate system for the impinging plate is represented in Fig. 2, and for the inclined surface a coordinate system (x'-y'-z') is used, which is rotated by 12° around the z axis relative to the impinging plate system, so that x' and y' are perpendicular and tangent to the inclined plate, respectively.

For the impinging plate, Fig. 23 (a) and more clearly shown in the solid line of Fig. 24, the normalized stress τ_{xy} shows a minimum value (in magnitude) at the stagnation line (it is actually zero, but since we are using a quarter of the domain, the first cell center is outside the symmetry plane and the stress there is small, but non-zero). Then, the stress progressively increases until $y/H = 0.8$, the location of the end of the recirculation zone attached to the inclined wall. The separated flow region attached to the inclined wall

reduces the open area for the main flow (the cross section where the fluid moves forward) and this is felt also on the impinging plate. So, regardless of the size of the recirculation zone, the main flow open area decreases, and mass conservation forces an acceleration of the main flow, which increases the transverse gradient of streamwise velocity ($\partial v/\partial x$ in this region) and consequently the shear stresses τ_{xy} on the impinging plate. At the end of the recirculation, there is a local increase of the open area and by the same reasoning a local decrease of the shear stress, which exhibits a local minimum. Henceforth, the progressive decrease of the flow area due to the inclined wall, progressively accelerates the flow and increases the velocity gradient and the shear stress. The inclined wall ends at about $y/H = 3.5$ and becomes parallel to the impinging plate, thus defining the exit rectangular channel of constant cross section. There is a second local stress maximum at the end of the converging channel, because the flow does not change direction as

Table 3
Recirculation lengths (L_R/H) function of Reynolds number, exit channel thickness and angle of the slopping wall.

Height	H = 2mm			H = 4mm			H = 6mm		
	Re = 275	Re = 680	Re = 1088	Re = 275	Re = 680	Re = 1088	Re = 275	Re = 680	Re = 1088
α (°)									
0	0.48	0.90	1.46	0.85	1.55	2.33	1.27	2.6	3.53
5	0.31	0.59	0.76	0.54	0.94	1.18	0.85	1.36	1.63
12	0.17	0.42	0.55	0.41	0.71	0.85	0.68	1.00	1.20
20	—	0.28	0.35	0.30	0.47	0.55	0.50	0.71	0.80
25	—	0.22	0.29	0.27	0.41	0.48	0.45	0.62	0.69
30	—	—	—	0.21	0.36	0.41	0.36	0.51	0.59
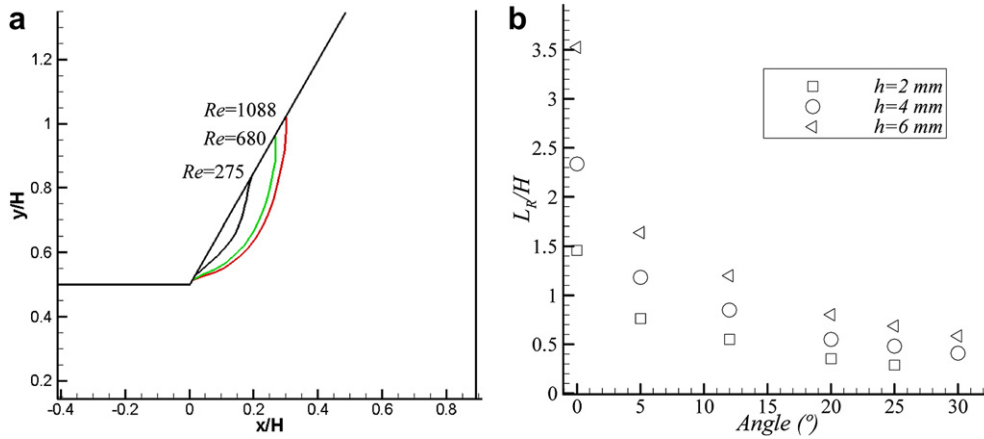
Fig. 22. Recirculation at the sloping wall and $z/W = 0$: a) shape of the separating streamline for $h = 6$ mm, $\alpha = 30°$ and $Re = 275$, 680 and 1088; b) Recirculation length for $h = 2$, 4 and 6 mm as a function of α and h for $Re = 1088$.

suddenly as the geometry itself due to flow inertia. Then, the velocity profile quickly becomes fully-developed and consequently the wall shear stress reaches a constant value except near the side wall where a boundary layer is developing.

At the inclined wall, Fig. 23 (b), the normalized stress $\tau_{x'y'}$ changes sign at the end of the separated flow region ($y'/H \approx 0.85$), after which the stress increases progressively until the end of the inclined wall ($y'/H = 3.25$) due to the accelerating flow and correspondingly higher velocity gradients. At $z'/H = 5.75$ and $y'/H = 1.5$ an oscillation of the contour is seen, which corresponds to the near side-wall jet. This oscillation decreases as the fluid moves downstream toward the end of the inclined wall and the near wall jet strength is reduced.

Fig. 24 compares the evolution of the normalized wall shear stress τ_{xy} along the impinging plate middle line for the inclined and the classical zero inclination cases, including also the effect of channel exit thickness. In the channel with an inclined plate the stress exhibits local maxima and one minimum related to the flow kinematics as discussed above, whereas in the absence of

inclination only the first maximum associated with the end of the recirculation is seen. Subsequently, the flow evolves to become fully-developed in the constant thickness channel and this is well shown in the monotonic variation of the stress to a constant value. For thicker channels the stresses are lower because of the lower wall shear rates.

In terms of pressure variation along the impinging plate, the highest pressure occurs at the stagnation point, where the jet flow changes direction (see Fig. 25(a) and (b)). Fig. 25b) shows profiles of pressure, normalized by the stagnation pressure, P_0, along the impinging plate and at $z/W = 0$, for different exit channel thicknesses and angles of inclination and in all cases the highest pressure also occurs at the stagnation point. For the configuration with $\alpha = 12°$, the pressure variation between $y/H = 0.5$ and $y/H = 2.0$ is quite small, showing that the pressure gradient is very weakly favorable. From there on, the pressure decreases continuously until the exit of the channel. For $y/H > 3.5$, the pressure gradient becomes nearly constant, which is characteristic of an almost fully-developed flow. Comparing the results for the two
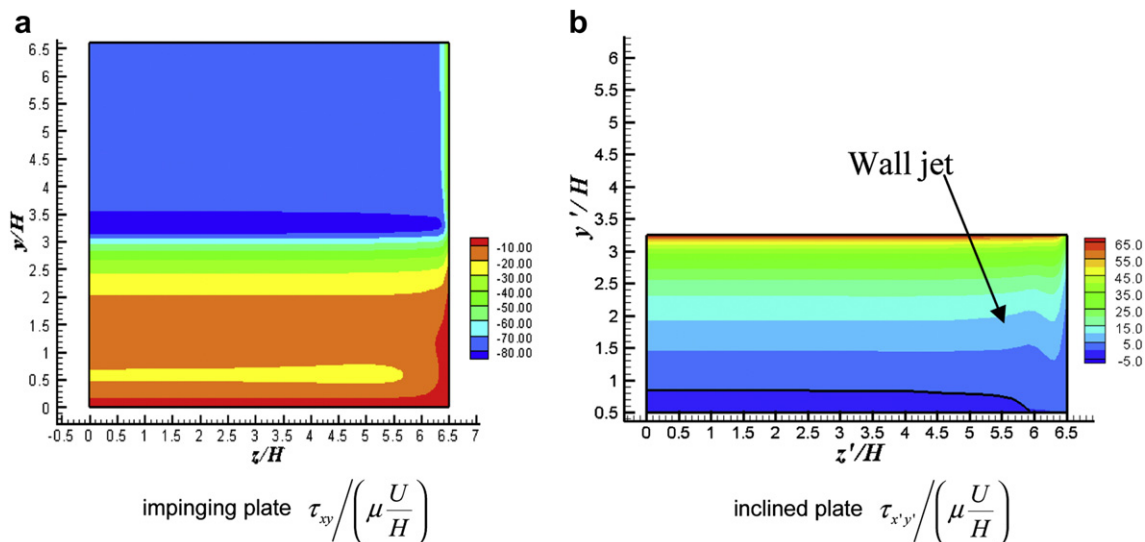
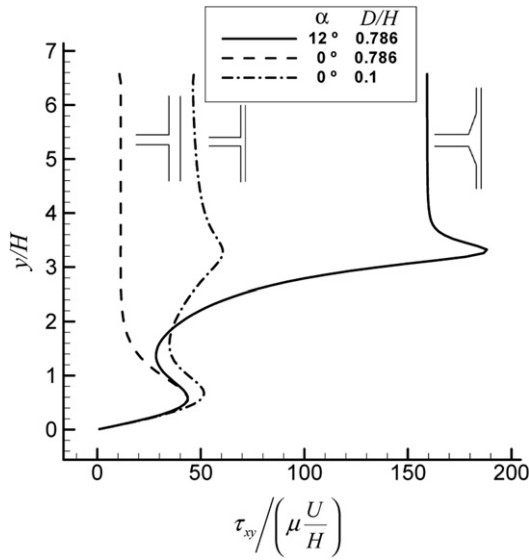**Fig. 23.** Contour of the shear stress for $Re = 275$: (a) along the impinging plate; (b) along the inclined wall.

Fig. 24. Variation of the shear stress with α and h ($D/H = 0.786$ and $D/H = 0.1$) along the impinging plate for $z/W = 0$ and $Re = 275$.

configurations with $\alpha = 0°$ and different exit channel thicknesses, the conclusion is that the flow develops faster the thicker the channel: for $D/H = 0.786$, the pressure gradient becomes constant for $y/H = 1$ while for $D/H = 0.1$, the pressure gradient becomes constant for $y/H > 3.5$.

Excess pressure loss is a key metric characterizing any flow field, and in this flow the dominant contribution to the pressure loss comes from the shear stress distribution along the impinging surface and in its neighborhood. In Fig. 26 we plotted the dimensionless excess pressure $(\Delta P/(1/2\rho U^2)) \times Re$ as a function of Reynolds number, i.e., the usual normalization of the pressure loss by inertia, multiplied by the Reynolds number. The excess pressure loss (ΔP) is determined from the computed pressure field, as follows: the energy equation between planes 1 and 2, located in regions of fully-developed flow (cf. Fig. 2 (b)), reads as

$$P_1 + \frac{1}{2}\rho\alpha_1 U_1^2 + \rho g z_1 = P_2 + \frac{1}{2}\rho\alpha_2 V_2^2 + \rho g z_2 + \Delta p_{F1} + \Delta p_{F2}$$
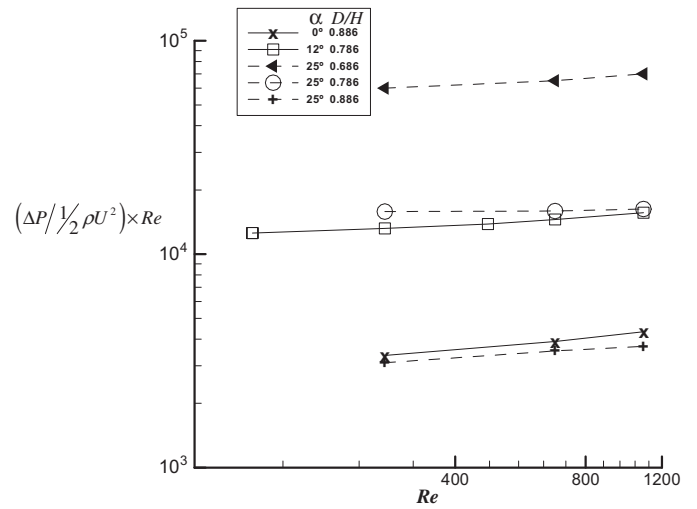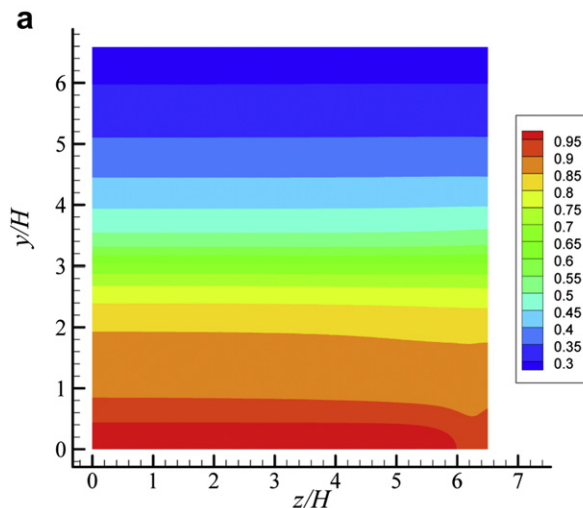$$+ \frac{1}{2}\rho\Delta P U_1^2 \qquad (5)$$

Fig. 26. Variation of the normalized excess pressure loss, $(\Delta P/1/2\rho U^2) \times Re$ with Reynolds number for several flow configurations.

where α_1 and α_2 stands for the profile shape factor for energy at planes 1 and 2 respectively.

After simplification, following the method of Oliveira and Pinho [25], we obtain the following extrapolated pressures at planes 01 and 02, respectively by fitting to pressure variations only along the fully-developed regions upstream and downstream of the sloped wall channel: $P_{01} \equiv P_1 - f_1 L_1 / D_{h1}\rho U_1^2/2$ and $P_{02} \equiv P_2 - f_2 L_2 / D_{h2}\rho V_2^2/2$. Defining the area ratio $\sigma \equiv A_1/A_2$, then ΔP is calculated using equation (6).

$$\Delta P = \frac{P_{01} - P_{02}}{\frac{1}{2}\rho U_1^2} + \alpha_1 - \alpha_2\sigma^2 \qquad (6)$$

For the various geometric configurations Fig. 26 shows that at the Reynolds numbers plotted the dimensionless pressure loss is in the transition between the low Reynolds number region, where ΔP is independent of Reynolds number, to the high Reynolds number region where it scales with Re. Additionally, ΔP increases with α and in inverse proportion to h.
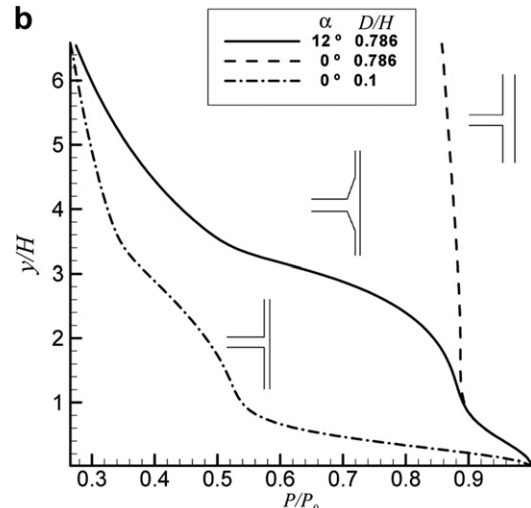

Fig. 25. Pressure variation along the impinging plate for $Re = 275$: (a) Pressure contour for $\alpha = 12°$; (b) normalized pressure profile for $z/W = 0$ as a function of α and h.

5. Conclusions

The flow field created by a laminar Newtonian liquid jet emanating from a fully-developed rectangular duct and impinging on a flat plate inside a cell confined by inclined plane walls was experimentally and numerically investigated in detail. For the numerical calculations a finite-volume method was used relying on at least second order differencing and interpolating schemes, whereas the experiments involved flow rate and pressure variation measurements, velocity measurements using LDA and flow visualization. The flow in the approach rectangular duct, having an aspect ratio of 13, was allowed to fully-develop prior to exiting the duct. Inside the duct and elsewhere, the flow was always symmetric in relation to the $z/W = 0$ and $y/H = 0$ center-planes.

The experiments, carried out at Reynolds numbers of 136 and 275, measured a separation flow region adjacent to the inclined walls for $Re>208$ and for $Re = 275$ there is a helical motion inside this separation region. The length of this recirculation zone decreased for decreasing Reynolds number.

For $Re = 275$, the separated flow along the sloping wall has a normalized length, L_R/H, equal to 0.35 in the central region of the cell and decreasing to zero at about $z/W = 0.95$, i.e., as the side wall is approached. This separation region does not exist along the full span of the cell, but only between $-0.95 \leq z/W \leq +0.95$, regardless of Reynolds number and thickness of the exit channel as found also from the numerical simulations. In addition, a three-dimensional effect was observed near the side walls and experimentally analysed in detail. The helical motion inside the separated flow region moves fluid particles from the center plane toward the side wall after leaving the flow recirculating region, where it merges with the main flow coming from the inlet channel thus creating a near side-wall jet detected by local velocity peaks.

The influences of the thickness of the exit channels (h) and of the angle of the sloping plane (α) upon the flow patterns inside the cell test section and other flow properties were also investigated. The recirculation length (L_R/H) was found to increase with h and in inverse proportion to α, while the spanwise component of the velocity inside the recirculation zone decreased with h, thus reducing the wavelength of the spiraling motion. The excess pressure loss was also computationally determined and found to scale with Reynolds number.

Acknowledgments

References

[1] M.A. Alves, P.J. Oliveira, F.T. Pinho, A convergent and universally bounded interpolation scheme for the treatment of advection, Int. J. Numer. Meth. Fluids 47 (2003) 665—679.

[2] A.S. Cavadas, 2008. "Hydrodynamic of confined impinging jets- Flow of Newtonian and Non-Newtonian fluids", PhD Thesis (in Portuguese), Faculdade de Engenharia da Universidade do Porto, Porto, Portugal.

[3] A. Chatterjee, An infinite series solution for creeping radial entrance flow of a newtonian fluid, AIChE J. 39 (1993) 1563—1568.

[4] A. Chatterjee, Newtonian radial entrance flow, AIChE J. 46 (2000) 462—475.

[5] A. Chatterjee, L.J. Deviprasath, Heat transfer in confined laminar axisymmetric impinging jets at small nozzle-plate distances: the role of upstream vorticity diffusion, Numer. Heat Transfer A: Appl. 37 (2001) 777—800.

[6] A. Chatterjee, S.C. Dhingra, S.S. Kapoor, Laminar impinging jet heat transfer with a purely viscous inelastic fluid, Numer. Heat Transfer, Part A: Appl. 42 (2002) 193.

[7] Q. Chen, V. Modi, Mass transfer in turbulent impinging slot jets, Int. J. Heat Mass Transfer 42 (5) (1999) 873—887.

[8] A.C. Cotler, E.R. Brown, V. Dhir, M.C. Shaw, Chip-level spray cooling of an LD-MOSFET RF power amplifier, IEEE Trans. components Packaging Technologies 27 (2004) 411—416.

[9] R.E. Franklin, J.M. Wallace, Absolute measurements of static-hole error using flush transducers, J. Fluid Mech. 42 (1970) 33—48.

[10] R. Gardon, J.C. Akfirat, The role of turbulence in determining the heat transfer characteristics of impinging jets, Int. J. Heat Mass Transfer 8 (1965) 1261—1272.

[11] R. Gardon, J.C. Akfirat, Heat transfer characteristics of impinging two-dimensional air jets, ASME J. Heat Transfer 65 (1966) 101—108.

[12] S.V. Garimella, R.A. Rice, Confined and submerged liquid jet impingement heat transfer, ASME J. Heat Transfer 117 (1995) 871—877.

[13] R.I. Issa, P.J. Oliveira, Numerical predictions of phase separation in two-phase flow through T-junctions, Comput. Fluids 23 (1994) 347—372.

[14] J. Kim, Spray cooling heat transfer, Int. J. Heat Fluid Flow 28 (2007) 753—767.

[15] M. Korger, F. Krizek, Mass-transfer coefficient in impingement flow from slotted nozzles, Int. J. Heat Mass Transfer 9 (1966) 337—344.

[16] D. Lytle, B. Webb, Air jet impingement heat transfer at low nozzle-plate spacings, Int. J. Heat Mass Transfer 37 (1994) 1687—1697.

[17] H. Martin, Heat and mass transfer between impinging gas jets and solid surfaces, Adv. Heat Transfer 13 (1977) 1—60.

[18] A. Melling, J.H. Whitelaw, "Turbulent flow in a rectangular duct, J. Fluid Mech. 78 (1976) 289—315.

[19] J.M. Miranda, J.B.L.M. Campos, Impinging jets confined by a conical wall: laminar flow predictions, AIChE J. 45 (1999) 2273—2285.

[20] J.M. Miranda, J.B.L.M. Campos, Concentration polarization in a membrane placed under an impinging jet confined by a conical wall - a numerical approach, J. Membr. Sci. 182 (2001) 257—270.

[21] V. Narayanan, J. Seyed-Yagoobi, R.H. Page, An experimental study of fluid mechanics and heat transfer in an impinging slot jet flow, Int. J. Heat Mass Transfer 47 (2004) 1827—1845.

[22] N.-T. Nguyen, S.T. Wereley, Fundamentals and applications of microfluidics, Integrated Microsystems Series, second ed., Artech House, 2006.

[23] K. Nishino, M. Samada, K. Kasuya, K. Torii, Turbulence statistics in the stagnation region of an axisymmetric impinging jet flow, Int. J. Heat Fluid Flow 17 (1996) 193—201.

[24] P.J. Oliveira, 1992, "Computer modeling of multidimensional multiphase flow and application to T-junctions", Ph.D. thesis, Imperial College, London, U.K.

[25] P.J. Oliveira, F.T. Pinho, Pressure drop coefficient of laminar Newtonian flow in axisymmetric sudden expansions, Int. J. Heat Fluid Flow 18 (1997) 518—529.

[26] M. Panão, 2008. "Experiments on impinging intermittent sprays" PhD Thesis, Universidade Técnica de Lisboa, Lisboa, Portugal.

[27] S.V. Patankar, Numerical Heat Transfer and Fluid Flow, Hemisphere Publishing Company, Washington, 1980.

[28] M. Perić, 1985, "A finite volume method for the prediction of three-dimensional fluid flow in complex duct", Ph.D. thesis, Imperial College, London, U.K.

[29] W.R. Quinn, Turbulent free jet flows issuing from sharp-edged rectangular slots: the influence of slot aspect ratio, Exp. Therm. Fluid Sci. 5 (1992) 203—215.

[30] J. Sakakibara, K. Hishida, M. Maeda, Vortex structure and heat transfer in the stagnation region of an impinging plane jet (simultaneous measurements of velocity and temperature fields by digital particle image velocimetry and laser- induced fluorescence), Int. J. Heat Mass Transfer 40 (13) (1997) 3163—3176.

[31] J. Senter, C. Solliec, Flow field analysis of a turbulent slot air jet impinging on a moving flat surface, Int. J. Heat Fluid Flow 28 (2007) 708—719.

[32] R. Shaw, The influence of hole dimensions on static pressure measurements, J. Fluid Mech. 7 (1960) 550—564.

[33] I. Sezai, A.A. Mohammad, Three dimensional simulation of laminar impinging rectangular jets, flow structure, and heat transfer, Trans. ASME J. Heat Transfer 121 (1999) 50—56.

[34] J.P. Van Doormal, G.D. Raithby, Enhancements of the SIMPLE method for predicting incompressible fluid flows, Numer. Heat Transfer 7 (1984) 147—163.

[35] M. Van Dyke, Entry flow in a channel, J. Fluid Mech. 46 (1970) 813—823.

[36] R. Viskanta, Heat transfer to impinging isothermal gas and flame jets, Exp. Thermal Fluid Sci. 6 (1993) 111—134.

[37] J. Vrentas, J.L. Duda, Flow of a Newtonian fluid through a sudden contraction, Appl. Sci. Res. 28 (1973) 241.

[38] B. Webb, C.F. Ma, Single-phase liquid jet impingement heat transfer, Adv. Heat Transfer 26 (1995) 105—217.

[39] F.M. White, Viscous Fluid Flow, second ed.. McGraw-Hill, 1991.

[40] D.H. Wolf, R. Viskanta, F.P. Incropera, Local convective heat transfer from a heated surface to a planar jet of water with non-uniform velocity profile, ASME J. Heat Transfer 112 (1990) 899—905.

[41] G. Yang, M. Choi, J.S. Lee, An experimental study of slot jet impingement cooling on concave surface: effects of nozzle configuration and curvature, Int. J. Heat Mass Transfer 42 (12) (1999) 2199—2209.

[42] D.W. Zhou, S.J. Lee, Forced convective heat transfer with impinging rectangular jets, Int. J. Heat Mass Transfer 50 (2007) 1916—1926.